JUAN PEDRO MELLADO[1] BJORN STEVENS[2]
HEIKO SCHMIDT[3] NORBERT PETERS[4]

Buoyancy-reversal in cloud-top mixing layers[5]

[1]Institut für Technische Verbrennung, RWTH Aachen,
e-mail: jpmellado@itv.rwth-aachen.de
[2]Max Planck Institute for Meteorology, Hamburg,
bjorn.stevens@zmaw.de
[3]Zuse Institute Berlin (ZIB) and Freie Universität Berlin, Department of Mathematics and
Computer Science,
e-mail: heischmi@math.fu-berlin.de
[4]Institut für Technische Verbrennung, RWTH Aachen,
e-mail: N.Peters@itv.rwth-aachen.de
[5]**submitted to the Quarterly Journal of the Royal Meteorological Society**

ZIB-Report 08-50 (Dezember 2008)

Buoyancy-reversal in cloud-top mixing layers

J.P. Mellado, B. Stevens, H. Schmidt, and N. Peters

January 12, 2009

Abstract

A theoretical and numerical small-scale study of the evaporative cooling phenomenon that might appear in the stratocumulus-topped boundary layers is presented. An ideal configuration of a cloud-top mixing layer is considered as defined by two nonturbulent horizontal layers, stably stratified and with buoyancy reversal within a certain range of mixture fractions due to the evaporative cooling. Linear stability analysis of the shear-free configuration is employed to provide a new interpretation of the buoyancy reversal parameter, namely, in terms of a time-scale ratio between the unstable and the stable modes of the system. An incompressible high-order numerical algorithm to perform direct numerical simulation of the configuration is described and two-dimensional simulations of single-mode perturbations are discussed. These simulations confirm the role of the different parameters identified in the linear stability analysis and show that convoluted flow patterns can be generated by the evaporative cooling even for the low levels of buoyancy reversal found in stratocumulus clouds. They also show that there is no enhancement of entrainment of upper layer fluid in the shear-free configuration, and mixing enhancement by the evaporative cooling is restricted to the lower layer.

Keywords: stratocumulus; free convection; free turbulent flows

1   Introduction

The importance of the physical phenomena occurring at the stratocumulus top of the planetary boundary layer is as well recognized as poorly understood [cf. Stevens (2002) and discussion therein]. This region normally separates a lower layer of turbulent flow from an upper layer of subsiding air that is approximately laminar, giving rise to turbulent entrainment, external intermittency and a turbulent/nonturbulent transition region, the so-called turbulence interface. This problem by itself, without any consideration of the cloud physics, is still a matter of basic research in the field of free turbulent flows, in spite of its importance and long-standing recognition (Corrsin and Kistler, 1955; Fernando, 1991; Dimotakis, 2005; Hunt *et al.*, 2006). When the idiosyncrasies of the cloud, in this case stratocumulus, are added to it, the difficulty of the problem is almost overwhelming. However, accurate models of related quantities, like an entrainment rate or the subgrid scale terms in large eddy simulations, are necessary due to the role that these stratocumulus-top regions, of the order of meters or tens of meters, play in larger scale dynamics. In addition to the physical complexity of

the problem, the range of scales it embodies confounds brute force attempts to numerically explore the interplay between turbulent processes at the cloud top and those within the turbulent layer as a whole. Stevens (2002) reviews these issues and, as a part of the conclusion, advocates for the study of smaller-scale similar/related simplified more-specific problems that would allow us to gain insight into the more general and more complex system. The authors adopt this approach in this paper and study in detail one aspect of the cloud-top mixing, namely, the role of latent heat effects.

Latent heat effects are expected to be important because of the evaporative cooling caused by the mixing between the lower cooler and supersaturated layer and the upper warmer and unsaturated layer, which in some cases can lead to buoyancy reversal. The possibility of a resulting instability, the so-called cloud-top entrainment instability, which could ultimately break the cloud deck, remains an important and largely unresolved question (Randall, 1980; Deardorff, 1980; Kuo and Schubert, 1988; Grabowski, 1995; Wunsch, 2003; Yamaguchi and Randall, 2008).

Among the great number of studies focused on buoyancy reversal in cloud-topped layers, the series of papers by Shy and Breidenthal (1990), Siems *et al.* (1990) and Siems and Bretherton (1992) merit special attention. Shy and Breidenthal (1990) explored the effects of buoyancy reversal in a laboratory system (tank) consisting of methanol, ethylene glycol, salt and water, and characterized by two parameters: D, which measures the ratio of the maximum density of the mixture to the density difference of the unmixed fluids; and χ_m, the mixture fraction at which that maximum density occurs. Siems *et al.* (1990) present two-dimensional numerical simulations of this two-layer configuration without explicit subgrid scale modeling using a second-order algorithm. The evolution of the system is then described in terms of the stream-function and the mixture fraction χ for the case of discrete initial perturbations in the form of a buoyancy anomaly. Although this low-order scheme is too dissipative and leads to an almost laminar structure of the reversing system for the case $D = 0.05$, which is representative of real stratocumulus, their study was the first to recognize the applicability of direct numerical simulation (DNS) to this problem, as only DNS attempts to explicitly represent mixing processes and hence the scales at which latent heating effects are realized. These numerical studies were extended by Siems and Bretherton (1992) who tried to span the range between the laboratory scale, comparing with Shy and Breidenthal (1990) by using single-vortex initial conditions, and the atmospheric scale, using multiple-vortices initialization. A principal finding of these studies is the identification of a critical buoyancy reversal parameter D of order unity beyond which a qualitative change of the flow (a runaway in the entrainment of dry fluid from the upper layer or a sustained increase of kinetic energy despite the viscous dissipation) becomes evident. Actual cloud-top conditions typically have $D \ll 1$, which leads them to conclude that buoyancy reversal alone is not likely to destabilized the cloud layer as a whole.

In this study we build on the results of this previous work by exploring two open questions. First, although the parameter D can be easily introduced based on dimensional analysis, does it lend itself to a deeper physical interpretation? This is the topic of section 3, where a linear stability analysis is presented and used to interpret the buoyancy reversal parameter D in terms of a ratio between the growth rates of the unstable and stable modes. Second, to what extent is

the argument, that small values of D do not destabilize the system as a whole, an artifact of the stabilizing influence of the low-order numerics used by Siems *et al.* (1990) and Siems and Bretherton (1992)? To answer this question, a high-order numerical algorithm based on sixth-order compact schemes in space and a fourth-order five-step Runge-Kutta in time is described in section 4. Two-dimensional simulations are discussed in section 5 to extend the previous linear study into the nonlinear regime, showing the complicated pattern of mixing introduced by the buoyancy reversal—even for values $D \simeq 0.05$. At the same time, these simulations are used to validate the numerical algorithm and to further study the flow for the geophysically interesting case of $0 < D \ll 1$; in particular, statistics related to the mixture fraction and the energy budget are presented and discussed.

2 Formulation

The geometry considered is a two-layer system with the upper nonturbulent layer warmer and unsaturated and the lower one, also nonturbulent, cooler and supersaturated, gravity acting downwards. It is distinguished from (and simpler than) the cloud-top mixed layers (Lilly, 1968), in which the bottom layer is turbulent. It is therefore an idealized problem and will be referred to as cloud-top mixing layer, being shear-driven if Kelvin-Helmholtz instability dominates, buoyancy-driven if buoyancy reversal instability dominates, or a mixture of both. Only the shear-free configuration will be discussed in this paper.

Assuming that the liquid water phase can be represented as a continuum with the same diffusivity as the vapor, for low Mach number conditions the transport equations for the total water content and the enthalpy reduce to the advection-diffusion equation. Given equal thermal and mass diffusivities and with appropriate boundary and initial conditions the calculation of both can be represented in terms of the evolution of a single conserved scalar field, the mixture fraction $\chi(\mathbf{x}, t)$ satisfying the same advection-diffusion equation. In a two-layer system as we have here, the mixture fraction can be chosen to indicate the relative amount of mass of the fluid particle that originates from the upper layer. If thermodynamic equilibrium is assumed, the value of χ at each point and time determines completely the thermodynamic state of the fluid particle, in particular it provides the density as $\rho(\mathbf{x}, t) = \rho^e(\chi(\mathbf{x}, t))$ for a function $\rho^e(\chi)$ to be given.

In the Boussinesq limit with constant transport coefficients the governing equations are then

$$\frac{\partial \mathbf{v}}{\partial t} + \nabla \cdot (\mathbf{v} \otimes \mathbf{v}) = -\nabla p + \nu \nabla^2 \mathbf{v} + b\mathbf{k}$$
$$\nabla \cdot \mathbf{v} = 0 \tag{1}$$
$$\frac{\partial \chi}{\partial t} + \nabla \cdot (\mathbf{v}\chi) = \kappa \nabla^2 \chi$$

where the buoyancy is

$$b = \frac{\rho_0 - \rho}{\rho_0} g \ . \tag{2}$$

In the equations above, p is a modified pressure divided by the reference density, the kinematic viscosity is ν, κ is the scalar diffusivity and g represents the

magnitude of the gravity force, which is assumed constant and acting downwards along the vertical direction Oz, i.e. $\mathbf{g} = -g\mathbf{k}$. Flow variables from the upper layer, where $\chi = 1$ will be denoted by the subscript 1, and subscript 0 will correspond to the lower layer, where $\chi = 0$. The parameter $b_1 = g(\rho_0 - \rho_1)/\rho_0$ quantifies the strength of the stable inversion. Positively buoyant means $b > 0$ and the volumetric force is then directed upward along $\mathbf{k}$.

The function $b^e(\chi)$, or equivalently $\rho^e(\chi)$, remains to be characterized to obtain the volumetric force from the relation $b(\mathbf{x}, t) = b^e(\chi(\mathbf{x}, t))$. The first parameter entering is the density difference across the layer $\rho_0 - \rho_1$, which is equivalent to a buoyancy value b_1 already introduced above. If the density were a linear function of the scalar, i.e. $\rho = \rho_0 + \chi(\rho_1 - \rho_0)$, then $b^e(\chi) = b_1\chi$. When a phase change occurs and buoyancy reversal is present, linear thermodynamic analysis for a small density difference $\rho_0 - \rho_1$ shows that this function can be well approximated by a piecewise-linear profile, characterized by a maximum density ρ_m at a particular mixture fraction value χ_m that is fixed by the initial data. This maximum density is introduced in the problem through the nondimensional buoyancy reversal parameter (Shy and Breidenthal, 1990)

$$D = \frac{\rho_m - \rho_0}{\rho_0 - \rho_1} = -\frac{b_m}{b_1} \ . \tag{3}$$

Figure 1 shows the function $b^e(\chi)/b_1$ for the cases described in Table 1 (to be discussed later in section 5), along with the exact equilibrium solution given by a polynomial fit to the vapor pressure function (Flatau $et\ al.$, 1992). The approximate piecewise-linear behavior is clearly revealed in that figure.
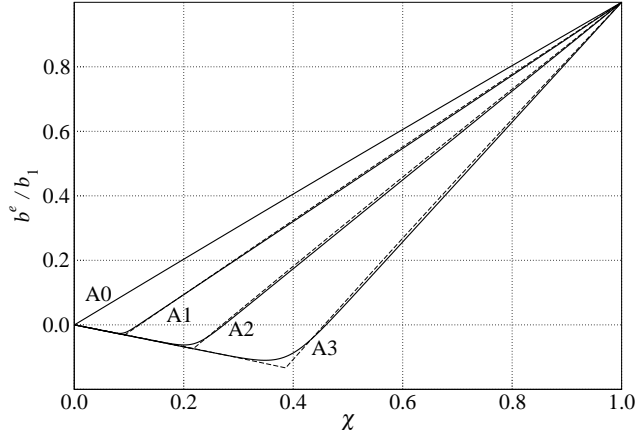

Figure 1: Nondimensional buoyancy mixing function for data in Table 1: dashed, exact thermodynamic equilibrium; solid, approximation Eq. (4).

The discontinuity in the derivative observed in those curves at χ_m, which corresponds to just saturation conditions, needs to be smoothed if the high-order schemes normally employed in DNS and later described are to be used, since they are not monotone and the derivative of the momentum equation is needed for the pressure equation. Therefore, the buoyancy function is approximated as

$$\frac{b^e(\chi)}{b_1} = -\frac{D}{\chi_m}\chi + \left(\frac{1+D}{1-\chi_m} + \frac{D}{\chi_m}\right)\delta_s \ln\left[\exp\left(\frac{\chi - \chi_m}{\delta_s}\right) + 1\right] \ , \tag{4}$$

which corresponds to the profile of the derivative $db^e/d\chi$ following a hyperbolic tangent between two different levels and centered at χ_m (see also Fig. 1). Mixture fractions smaller than $(\chi_m + D)/(1 + D)$ are negatively buoyant. Numerical studies performed to calculate the influence of δ_s on growth rates are presented in section 5 and show that a smoothing parameter defined by $\delta_s = \chi_m/16$ leads to deviations of less than 2%.

The equations are to be solved in a rectangular domain assuming periodicity in the horizontal directions Ox and Oy. The boundary conditions imposed at the top and the bottom are zero normal velocity and zero normal derivative of the horizontal velocities and the scalar field χ. The Neumann boundary conditions for the Poisson equation for the pressure at the top and the bottom are then (Gresho, 1991)

$$\frac{\partial p}{\partial z} = \nu \frac{\partial^2 w}{\partial z^2} + b \,, \tag{5}$$

where the boundary conditions on the velocity have been already applied and w is the vertical velocity. Additionally, one reference value of p (irrelevant for the flow) has to be given at one point.

If there is a velocity-scale U_0 externally imposed (e.g. from a mean shear or from a turbulent state in one of the layers) with a length-scale L_0, then dimensional analysis shows that the general solution can be written in the form

$$\frac{\mathbf{v}(\mathbf{x},t)}{U_0} = f(\frac{\mathbf{x}}{L_0}, \frac{tU_0}{L_0}; Re, Pr, Ri, \chi_m, D, \frac{a}{L_0}, \frac{\delta}{L_0})$$

$$\chi(\mathbf{x},t) = g(\frac{\mathbf{x}}{L_0}, \frac{tU_0}{L_0}; Re, Pr, Ri, \chi_m, D, \frac{a}{L_0}, \frac{\delta}{L_0}) \tag{6}$$

where the reference Reynolds and Richardson numbers are $Re = L_0 U_0/\nu$ and $Ri = b_1 L_0/U_0^2$, respectively, and the Prandtl number is $Pr = \nu/\kappa$. An amplitude a of the initial perturbation of the interface has been assumed along with a initial thickness δ of the initial mean scalar profile of χ.

If there is no velocity-scale externally imposed, then b_1 and L_0 can be used to write

$$\frac{\mathbf{v}(\mathbf{x},t)}{\sqrt{L_0 b_1}} = f(\frac{\mathbf{x}}{L_0}, t\sqrt{\frac{b_1}{L_0}}; Gr, Pr, \chi_m, D, \frac{a}{L_0}, \frac{\delta}{L_0})$$

$$\chi(\mathbf{x},t) = g(\frac{\mathbf{x}}{L_0}, t\sqrt{\frac{b_1}{L_0}}; Gr, Pr, \chi_m, D, \frac{a}{L_0}, \frac{\delta}{L_0}) \tag{7}$$

as the general solution to the nondimensional equations

$$\frac{\partial \mathbf{v}}{\partial t} + \nabla \cdot (\mathbf{v} \otimes \mathbf{v}) = -\nabla p + \frac{1}{Gr^{1/2}} \nabla^2 \mathbf{v} + b\mathbf{k}$$

$$\nabla \cdot \mathbf{v} = 0 \tag{8}$$

$$\frac{\partial \chi}{\partial t} + \nabla \cdot (\mathbf{v}\chi) = \frac{1}{Gr^{1/2} Pr} \nabla^2 \chi$$

which introduces the reference Grashof number (common in free convection flows, e.g. Tritton (1988)) as $Gr = L_0^3 b_1/\nu^2$. Other combinations of these nondimensional groups might be preferable for different particular configurations, as will be done in section 5.

The unperturbed initial condition is assumed to correspond to the enthalpy and total specific humidity following an error function profile, which is a solution

of the purely diffusive equations. This is imposed in the current formulation by prescribing the mixture fraction at the initial time as

$$\chi_i(z) = \frac{1}{2} \left[1 + \text{erf} \left(\frac{z}{2\delta} \right) \right] \ .$$ (9)

The origin of the coordinate system is taken at the interface and the thickness of this interface in terms of χ is parameterized by δ. Evaporative cooling (Eq. (4) and Fig. 1) implies then a three layer structure in the density field, with a middle heavier layer of an approximate thickness of order $\delta(\chi_m + D)/(1+D)$. The effect of a perturbation of magnitude a to this configuration is further explored in the following sections.

3 Linear stability analysis

This section discusses the linear stability analysis of a three-layer density field without mean shear. The initial perturbation a is assumed to be small enough, i.e. $a/[\delta(\chi_m + D)/(1+D)] \ll 1$; stronger perturbations falling outside this linear regime will be considered in section 5 via numerical simulations. The basic configuration is depicted in Fig. 2. It represents an idealized buoyancy reversal system, substituting the smooth density variation by a stepwise profile. The analysis is done assuming constant density in each of the layers and irrotational flow. This problem, for the case of a two-layer system, is described in many text books (e.g. Turner (1973)) and the general multilayer case has been also discussed in the literature (Yang and Zhang, 1993). A three-layer system like the one here has received less attention; experimental investigations are reported by Jacobs and Dalziel (2005) but with a different stratification ($\rho_1 > \rho_0$ instead of the case $\rho_1 < \rho_0$ of interest here). It is therefore of interest to study this three-layer basic problem in detail.
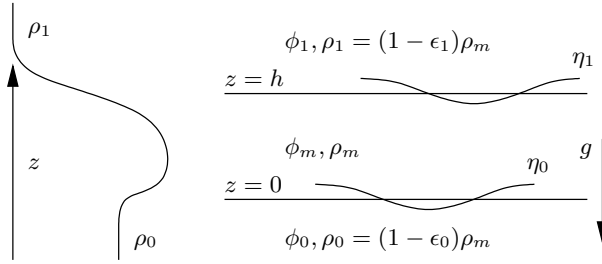

Figure 2: Vertical density profile (left) and three-layer idealized configuration (right) representing the buoyancy reversal state by a density ρ_m greater than ρ_0 and ρ_1.

Let us denote with ϕ_j the velocity potential in each of the layers, which satisfies the Laplace equation, and with η_0 and η_1 the displacement of each interface with respect to the reference position, separated by a distance h (see Fig. 2). The boundary conditions for the linearized problem consist of the

kinematic condition,

$$\frac{\partial \phi_0}{\partial z} = \frac{\partial \phi_m}{\partial z} = \frac{\partial \eta_0}{\partial z} \ , \qquad \text{at } z = 0 \ ,$$

$$\frac{\partial \phi_1}{\partial z} = \frac{\partial \phi_m}{\partial z} = \frac{\partial \eta_1}{\partial z} \ , \qquad \text{at } z = h \ ,$$

and the dynamic condition of continuity of pressure at the interfaces,

$$\frac{\partial}{\partial t}(\rho_m \phi_m - \rho_0 \phi_0) + (\rho_m - \rho_0)g\eta_0 = 0 \ , \qquad \text{at } z = 0 \ ,$$

$$\frac{\partial}{\partial t}(\rho_1 \phi_1 - \rho_m \phi_m) + (\rho_1 - \rho_m)g\eta_1 = 0 \ , \qquad \text{at } z = h \ ,$$

having used the linearized Bernoulli equation in each of the three layers $\rho_j \partial \phi_j / \partial t +$
$p_j + \rho_j gz = G_j$, with suitable functions $G_j(t)$.

Solutions are sought in the form

$$\phi_j = f_j(z) \exp(ikx + \sigma t) \ , \qquad j = 1, 2, 3 \ . \tag{10}$$

The boundary condition on the normal velocity at the interfaces implies that
$\eta_0 = A_0 \exp(ikx + \sigma t)$ and similarly for η_1, along with relations between $f'(z)$
at those interfaces. Solving the Laplace equations for ϕ_j we obtain

$$\begin{pmatrix} f_0 \\ f_m \\ f_1 \end{pmatrix} = e^{-kz} \begin{pmatrix} 0 \\ a_m \\ a_1 \end{pmatrix} + e^{kz} \begin{pmatrix} b_0 \\ b_m \\ b_1 \end{pmatrix}$$

where the integration constants can be expressed in terms of $A_0 \sigma / k$ and $A_1 \sigma / k$.
Substituting these results in the boundary conditions for the pressure, we obtain
a homogeneous linear system for the variables A_0 and A_1, with the characteristic
polynomial

$$\rho_m^2 = \left[\sinh(kh) \left(\frac{gk}{\sigma^2}(\rho_m - \rho_0) - \rho_0 \right) - \rho_m \cosh(kh) \right]$$

$$\times \left[\sinh(kh) \left(\frac{gk}{\sigma^2}(\rho_1 - \rho_m) - \rho_1 \right) - \rho_m \cosh(kh) \right] \ .$$

The eigenvalue is defined as the square of the growth rate, σ^2. There are two
eigenvalues and therefore two normal modes for each given wavenumber k (Yang
and Zhang, 1993).

Let us now introduce the ratios ϵ_0 and ϵ_1, such that

$$\rho_1 = \rho_m(1 - \epsilon_1) \ ,$$

$$\rho_0 = \rho_m(1 - \epsilon_0) \ . \tag{11}$$

Then, the characteristic polynomial becomes

$$1 = e^{2kh} - e^{kh} \sinh(kh) \left[\epsilon_0 + \epsilon_1 + \frac{gk}{\sigma^2}(\epsilon_0 - \epsilon_1) \right]$$

$$+ \epsilon_0 \epsilon_1 \sinh^2(kh) \left[1 - \left(\frac{gk}{\sigma^2} \right)^2 \right] \ . \tag{12}$$

7

For the case $\epsilon_0\epsilon_1 \neq 0$, the quadratic equation leads to

$$\frac{\sigma^2}{gk} = \frac{\epsilon_0\epsilon_1}{(\epsilon_1 - \epsilon_0)}\frac{1 - e^{-2kh}}{1 \pm \sqrt{\Delta}} \ ,$$

$$\Delta = 1 + 4\frac{\epsilon_0\epsilon_1}{(\epsilon_1 - \epsilon_0)^2}(1 - e^{-2kh})$$

$$\times [(1 - \frac{\epsilon_0}{2})(1 - \frac{\epsilon_1}{2}) - \frac{\epsilon_0\epsilon_1}{4}e^{-2kh}]$$

In the Boussinesq limit $O(\epsilon_0), O(\epsilon_1) \ll 1$ and the previous equation simplifies to

$$\frac{\sigma^2}{gk} = \frac{\epsilon_0\epsilon_1}{(\epsilon_1 - \epsilon_0)}\frac{1 - e^{-2kh}}{1 \pm \sqrt{1 + 4\frac{\epsilon_0\epsilon_1}{(\epsilon_1 - \epsilon_0)^2}(1 - e^{-2kh})}} \ . \tag{13}$$
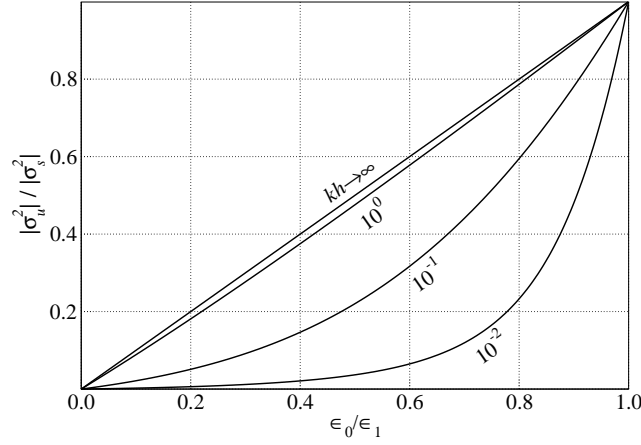

Figure 3: Ratio between the unstable and stable mode growth rates as a function of the density difference ratio and the nondimensional wavenumber kh in the Boussinesq limit $O(\epsilon_0), O(\epsilon_1) \ll 1$.

In our particular case, $0 < \epsilon_0 < \epsilon_1$, and there is always one unstable solution σ_u, corresponding to the positive sign in front of the square root, and one stable solution σ_s, corresponding to the negative sign. The physical system has therefore two time-scales, $|\sigma_u|^{-1}$ and $|\sigma_s|^{-1}$. Depending on the ratio $|\sigma_u|/|\sigma_s|$ the system will have fewer or higher number of oscillations before the unstable mode is appreciated. The ratio between the unstable and stable eigenvalue is always less that 1, increasing with ϵ_0/ϵ_1 as shown in Fig. 3. The dependence on the thickness of the unstable middle layer h occurs through the nondimensional wavenumber kh. For small values of kh, the unstable growth rate tends to zero whereas the stable solution tends to $\sigma^2 = -(\epsilon_1 - \epsilon_0)gk/2 \simeq -b_1 k/2$, this result corresponding to the oscillation of a two-layer system formed by layers 0 and 1. For large values of kh, both growth rates tend to that corresponding to two independent two-layer systems, one stable with eigenvalue $-\epsilon_1 gk/2$, the other one unstable with eigenvalue $\epsilon_0 gk/2$.

In case of $\epsilon_0 \ll \epsilon_1$, as we expect to have, the solutions to Eq. (13) are

$$\begin{aligned} \sigma_u^2 &\sim \ \epsilon_0 gk(1 - e^{-2kh})/2 \ , \\ \sigma_s^2 &\sim -\epsilon_1 gk/2 \ , \end{aligned} \tag{14}$$

which corresponds to an oscillation period much smaller than the timescale of the exponential growth of the unstable mode. The solution for σ_s corresponds to a stable two-layer configuration; the interface η_1 does not feel the small density difference at $z = 0$. The solution for σ_u corresponds to an unstable two-layer system with a wall at a height $z = h$; this no-penetration condition is consistent with the fact that the upper interface η_1 oscillates fast compared with characteristic time of the unstable layer, and only the mean position $z = h$ is felt by the interface η_0.

Equation 13 corresponds to the functional dependence anticipated by Eq. (7) which we derived from dimensional analysis. This can be made explicit by noting that the former equation can be written in terms of the ratio ϵ_0/ϵ_1, the buoyancy reversal parameter Eq. (3) is

$$D = \frac{\epsilon_0/\epsilon_1}{1 - \epsilon_0/\epsilon_1} \qquad (15)$$

and $b_1 = g(\epsilon_1 - \epsilon_0)/(1 - \epsilon_0) \simeq g(\epsilon_1 - \epsilon_0)$ in the Boussinesq limit, leading to

$$\frac{\sigma^2}{kb_1} = \frac{1}{4} \left[-1 \pm \sqrt{1 + 4D(1 + D)(1 - e^{-2kh})} \right] \qquad (16)$$

with h playing the role of the thickness δ and k the inverse of a characteristic length L_0. The stable solution corresponds again to the minus sign and the unstable to the plus sign. This result is valid for any value of D.

Equation 16 allows to compare the results obtained in the linear analysis with the discussion presented in Shy and Breidenthal (1990) and Siems and Bretherton (1992) about the role of the buoyancy reversal parameter D. In the first place, the instability condition $0 < \epsilon_0 < \epsilon_1$ translates with the new notation into $D > 0$, which corresponds to the buoyancy reversal instability criteria introduced by Shy and Breidenthal (1990). Our analysis shows that this instability reflects one of two modes of the system, the second one being stable. Second, the critical value $D \simeq 1$ is reported in Siems and Bretherton (1992) to characterize the transition between buoyancy reversal instability and a strong buoyancy reversal instability, which can lead ultimately to cloud-top entrainment instability. However, the present linear analysis does not support such a scenario and Fig. 3 depicts a rather smooth variation of the unstable growth rate with D. If the value $D = 1$ is substituted in Eq. (16) then the growth rate of the unstable mode is only a factor $\sqrt{2}$ smaller than the corresponding stable one, hence $D \simeq 1$ should be simply interpreted as the condition for both modes to have comparable growth rates. This result suggest that to the extent $D \simeq 1$ represents a transition in the experiments of Shy and Breidenthal (1990), it does so because of nonlinear interactions related to the manner in which they perturb the interface in the experiment. Finally, Eq. (16) shows the influence of the thickness h of the buoyancy reversal layer. For values small compare to the wavelength of the perturbation, the growth rates increase with kh, but asymptote to a constant after kh is of order one.

Last, the case $D \ll 1$ (previous limit $\epsilon_0 \ll \epsilon_1$) is of special interest because it occurs often in normal conditions at the top of the cloud deck. In this limit

$$\begin{aligned} \sigma_u^2 &\sim \quad kb_1 D(1 - e^{-2kh})/2 \;, \\ \sigma_s^2 &\sim -kb_1/2 \;, \end{aligned} \qquad (17)$$

9

and the ratio of growth rates depends on the square of this buoyancy reversal parameter

$$\frac{|\sigma_u|}{|\sigma_s|} \sim \sqrt{D(1 - e^{-2kh})} \; . \tag{18}$$

In brief, the linear stability analysis shows that the system is characterized by two modes, the stable one with a period of oscillation given by Eq. (16) (negative sign), depending on the strength of the stable stratification as $b_1 k$ and with corrections depending on D and the nondimensional wavenumber kh, and the unstable mode with a growth rate smaller than the stable one (see Fig. 3) and whose exact value is given by Eq. (16) (positive sign). Two time-scales appear thus naturally from the equations, and a clear physical interpretation of the parameter D for the case $D \ll 1$ typical of the stratocumulus top is obtained. The period of oscillation can be written as $2\sqrt{\pi}\sqrt{\lambda/b_1}$ if a wavelength $\lambda = 2\pi/k$ is introduced, and the characteristic time of the unstable mode scales as $D^{-1/2}$ times this oscillation period, according to Eq. (18), with a prefactor depending on the nondimensional layer thickness h/λ. For $D = 0.1$ the ratio of the growth rates is 0.3 and it increases monotonically with the thickness h, but asymptotically after $kh \simeq O(1)$.

4   Numerical algorithm

An incompressible code for solving the set of equations presented in section 2 has been derived from a previously existing finite-differences compressible code (Mellado *et al.*, 2008). The algorithm follows Wilson *et al.* (1998), in particular, it uses a fourth-order low-storage Runge-Kutta scheme for the time advancement (Williamson, 1980) and a sixth-order compact Padé schemes for the spatial derivatives (Lele, 1992) over a uniform grid, which provide the finite-difference approximation to the derivative of a scalar field p, e.g. along the Oz direction, by solving the linear systems $A_1 \delta_z p = B_1 p$ and $A_2 \delta_{zz} p = B_2 p$, for the first- and second-order derivative, $\delta_z p$ and $\delta_{zz} p$, respectively. The matrices A_i are tridiagonal and the matrices B_i are pentadiagonal and the 0.1% error in the phase speed occurs at about 6 points per wavelength. The scheme is one-sided at the nonperiodic boundaries (top and bottom).

The discrete Poisson equation for the pressure is written using Fourier decomposition inside the horizontal planes, which leads to

$$\delta_z \delta_z \hat{p}_{ij} - \lambda^2 \hat{p}_{ij} = \hat{g}_{ij} \; , \tag{19}$$

where $\hat{p}_{ij}$ is the vector formed by the horizontal Fourier modes $i = 0, \ldots, N_x/2 - 1$ and $j = -N_y/2 + 1, \ldots, N_y/2 - 1$ (modes $N_x/2$ and $N_y/2$ are set to zero) at each z-position , and

$$\lambda^2 = [f(2\pi i/N_x)/(\Delta x)]^2 + [f(2\pi j/N_y)/(\Delta y)]^2 \; . \tag{20}$$

The transfer function $f(\omega)$ of the first-order finite-difference operator needed in the equation above is (Lele, 1992)

$$f(\omega) = \frac{(14/9)\sin(\omega) + (1/18)\sin(2\omega)}{1 + (2/3)\cos(\omega)} \; . \tag{21}$$

The Neumann boundary conditions are obtained by Fourier transforming Eq. (5). For the case $\lambda = 0$ one of the Neumann boundary conditions has to be substituted by a Dirichlet one, and $\hat{p}_{00} = 0$ is used.

The difficulty resides in solving the sequence of discrete equations Eq. (19), since each one is a linear system with a full matrix of size $N_z \times N_z$. The problem can be simplified by introducing an approximation to the operator $\delta_z \delta_z$ which leads to a system easier to solve. For instance, using the second-order finite-difference operator δ_{zz}, we have

$$\delta_{zz} \hat{p}_{ij} - \lambda^2 \hat{p}_{ij} = \hat{g}_{ij} - R\hat{p} \,, \tag{22}$$

with $Rp = \delta_z \delta_z p - \delta_{zz} p = (A_1^{-1} B_1 A_1^{-1} B_1 - A_2^{-1} B_2)p$, R being a full matrix. Cook and Dimotakis (2001) solve an approximation to this equation by neglecting the term $R\hat{p}$ in their Rayleigh-Taylor turbulence simulations and solving the resulting pentadiagonal linear system, and the same approach is followed here. The error introduced by this step in solving the Poisson equation, due to the different truncation error between $\delta_z \delta_z$ and δ_{zz}, is easily analyzed in the case of periodic boundary conditions with help of the corresponding transfer functions. It is then observed that the error increases monotonically with the wavenumber and is of the order of 0.1% with 6 points per wavelength, which is consistent with the properties of the schemes used to calculate the derivatives of the equations. However, this step involves a nonzero dilatation error whose level depends on the resolution; the effects of this error will be discussed later in section 5.

Finally, the buoyancy term in the momentum equation is prescribed in terms of the deviation $b^e(\chi(\mathbf{x}, t)) - b^e(\chi_i(z))$, with χ_i from Eq. (9). It is well-known that any function $f(z)$ can be subtracted from $b(\mathbf{x}, t)$ with an appropriate redefinition of the scalar field p, and our particular choice reduces the gradient of p at the upper boundary to almost zero, which contributes to well-behaved boundary conditions.

5 Two-dimensional simulations

A series of single-mode two-dimensional simulations are now presented with the purpose of illustrating the buoyancy reversal instability within the nonlinear regime as a complement to the linear analysis discussed in the previous section. These simulations also serve to validate the incompressible code for later use in the three-dimensional turbulence studies. The linear stability analysis identifies the possible significance of each of the parameters involved in the problem, namely, a time-scale related to b_1, a second time-scale which can be further related to D, and a thickness h of the middle heavy layer. However, several assumptions underlying our linear analysis are not satisfied in reality: there is diffusion of the baroclinically produced vorticity, the shape of the initial density profile varies smoothly and there are finite amplitude effects. Therefore, it is necessary to investigate with two-dimensional simulations whether the conclusions derived previously hold in reality.

No mean shear is considered and the initial perturbation is set by displacing sinusoidally the isosurface $\chi = 0.5$ from the hydrostatic equilibrium over a wavelength λ with an amplitude $a/2$. This initial condition is different from the disk anomaly used by Siems *et al.* (1990) and the single vortex employed by

Table 1: Simulation series A. Buoyancy reversal parameter D defined by Eq. (15) and $b_1 = (\epsilon_1 - \epsilon_0)/(1 - \epsilon_0)g \simeq (\epsilon_1 - \epsilon_0)g$. Equation 11 defines ϵ_0 and ϵ_1 in terms of the densities. Pressure level 940 hPa and upper layer at 19.1 °C and $q_{t,1}$=1.50 g kg^{-1}.

	$q_{t,0}$ (g kg^{-1})	T_0 (°C)	$\epsilon_1 - \epsilon_0$ (10^{-2})	ϵ_0 (10^{-3})	D	χ_m
A0	8.0	10.5	2.54	-	-	-
A1	9.0	10.6	2.54	0.79	0.031	0.09
A2	10.0	10.8	2.54	1.89	0.074	0.22
A3	12.0	11.3	2.54	3.37	0.133	0.39

Siems and Bretherton (1992) but follows the common initialization employed in Rayleigh-Taylor configurations (Cook and Dimotakis, 2001; Mellado *et al.*, 2005), the initial mechanical energy being introduced only through potential energy. The Prandtl number is unity.

5.1 Mixture fraction

A first series of simulations is performed to obtained a qualitative description of the flow and to study resolution requirements for the numerical algorithm presented in the previous section. The geometrical parameters used are $\delta/\lambda = 0.025$, where δ is the thickness of the initial error function profile Eq. (9), and the amplitude of the sinusoidal displacement $(a/2)/\lambda = 0.1$. The reference box size in the vertical direction is 2λ; different sizes were also investigated (but not shown) to ensure that there are no finite-domain-size effects on the results presented here. The cases considered are described in Table 1, where A1 is the reference case and corresponds to field experimental data from DYCOMS-II (Stevens *et al.*, 2003). The thermodynamic state of the upper layer is kept fixed at $T_1 = 19.1$ °C and $q_{t,1} = 1.5$ g kg^{-1}, and the lower state is modified to increase the effect of buoyancy reversal as shown in Fig. 1. The case A0 does not retain evaporation, so that only the oscillating stable mode is present, and cases A2 and A3 consider an increasing buoyancy reversal imposed by means of a higher water content in the lower layer, keeping constant the density difference $\rho_0 - \rho_1$ so that the period of the stable mode $2\sqrt{\pi}\sqrt{\lambda/b_1}$ remains the same. The Boussinesq formulation only needs the values χ_m and D from this table.

Linear stability analysis has identified two time-scales in the problem. In this study we start from the stable case A0 and add increasingly the unstable mode, then it is reasonable to take $\sqrt{\lambda/b_1}$ as the reference time-scale for the nondimensionalization. The relevant length-scale is the thickness of the layer, a, which leads to a viscous time-scale a^2/ν. The reference Grashof number of the problem, defined in terms of the ratio between the two previous time-scales, is $Gr = a^4 b_1/(\nu^2\lambda)$, and a value $Gr = 6.4 \times 10^5$ is used in this first series of simulations. The mesh of size 512×1024 is uniform and with equal grid spacing in every direction. It is noted that high resolution is needed to retain accurately the structure of the buoyancy field represented in Fig. 1 within the viscous superlayer formed between nonturbulent outer regions and the turbulent zone that will develop in the center. In this respect, 6 points per vorticity thickness is normally used for a sixth-order compact scheme. The vorticity thickness of
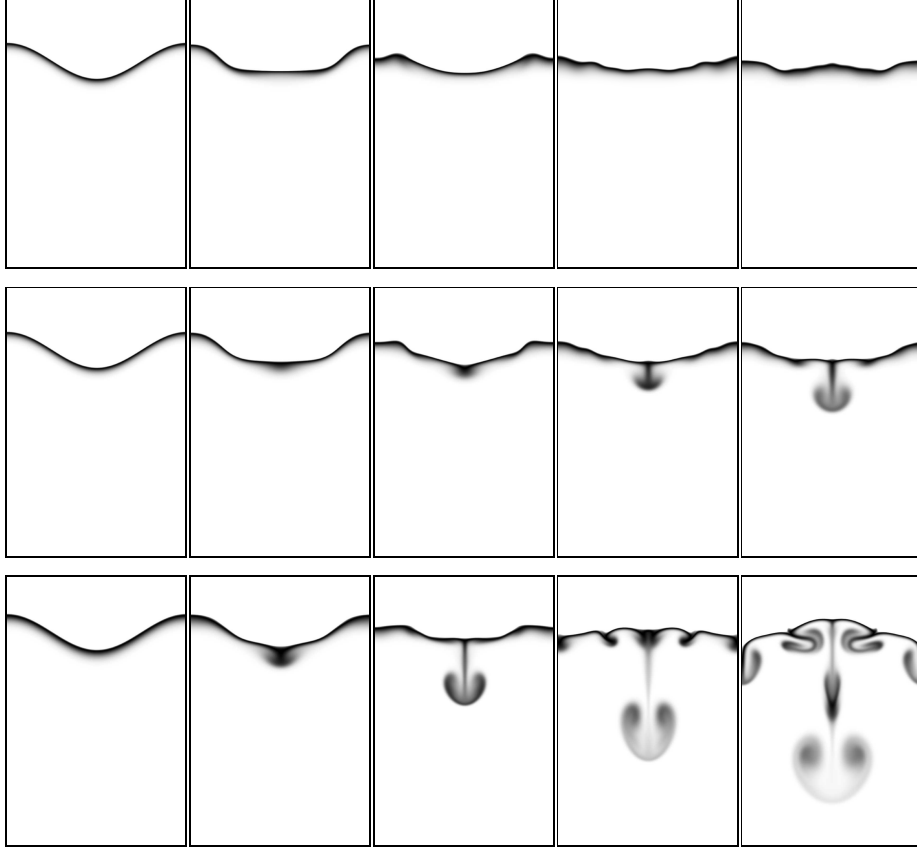
Figure 4: Negative buoyancy field for case A0 (top row), case A1 (middle row) and case A3 (bottom row) showing the evolution (left to right) starting from the initial condition and showing a frame every cycle of linear stable mode. Grashof number $Gr = 6.4 \times 10^5$.

a function f varying monotonously across a difference Δf between two levels is defined in terms of the maximum derivative by $\Delta f / f'_{\max}$. For the case of the error function profile Eq. (9) used here this vorticity thickness is 3.54δ and the resolution is then about 45 points per vorticity thickness of the initial mixture fraction field χ. However, the peak of the density field occurs within a fraction χ_m of the mixture fraction variation and the resolution of this buoyancy reversal layer can be as low as 10% of the complete viscous superlayer (see Table 1).

Figure 4 shows qualitatively the evolution of the negative buoyancy field (i.e. $b(\mathbf{x}, t) < 0$) every $2\sqrt{\pi}\sqrt{\lambda/b_1}$ time units. The stable case A0 is represented by $b^e(\chi(\mathbf{x}, t)) < 0$ using the function $b^e(\chi)$ corresponding to case A1 in order to compare the flow structure of both. The box height shown is only the lower 3/4 of the domain employed in the simulation. The results obtained in the linear stability analysis are reproduced here: superimposed on a standing gravity wave a falling finger, downdraft or spike, starts to form at the lowest point of the oscillation. This finger develops a mushroom shape typical of the Rayleigh-Taylor instability for small density differences (Sharp, 1984; Ramaprabhu and

Andrews, 2004). On top of this process, viscosity tries to eliminate the motion while diffusion spreads the buoyancy reversal by mixing the ambient moist air with the less moist air inside the falling finger.

The nonhomogeneous local mixing produced by the baroclinic production of vorticity at the oscillating inversion layer leads to the development of downdrafts at wavelengths smaller than the initial condition, which in turn enhances mixing at the core of the cloud-top mixing layer as compared to the nonevaporative case. This rearrangement of the buoyancy field is increasingly promoted as the buoyancy reversal is augmented either by larger values of D or χ_m, as noted by comparing cases A0, A1 and A3 in Fig. 4. The time evolution presents a pulsating behavior imposed by the stable mode, having the big initial central falling structure followed by a smaller one that appears in the last frame of Fig. 4. A certain amount of heavy fluid is pumped periodically into the lower layer, the falling finger pinches-off from the oscillating cetral layer and the feed of fluid from this central layer is stopped. More detailed study of the influence of each of these parameters is presented later. It is observed that buoyancy reversal enhances mixing in the lower layer, but there is no strong instability in the sense of a runaway behavior with a continuous tongue of falling upper fluid. This behavior agrees with the laboratory experiments by Shy and Breidenthal (1990) and with the numerical simulations of Siems *et al.* (1990) and Siems and Bretherton (1992), who refers to it as a evaporative enhancement of entrainment and is characteristic of small buoyancy reversal parameters $D < 1$.

The instability process in now quantified with help of the mixture fraction χ. Mean profiles $\bar{\chi}(z,t)$ for the case A3 are shown in Fig. 5 and the perturbation growing into the lower layer and depicted in Fig. 4 is easily observed in these mean profiles. This perturbation can be located by the point where the field χ departs from the constant value of the corresponding layer. For example, for the falling finger, we can take $\bar{\chi}$ and scan from the lowest boundary upward until the mean profile reaches a given threshold; the distance from this point to the center plane defines a height of the falling finger. Normally, a threshold of 1% of the difference between the two layers is used in turbulent Rayleigh-Taylor cases, but mixing in this problem is mainly reduced to the small fraction of χ affected by buoyancy reversal; the inset in Fig. 5 shows that $\bar{\chi}$ varies below 0.1 in the mixing region that forms in the lower layer. The threshold value 0.001 is therefore used.

The height of the falling finger as defined above is shown in Fig. 6 as a function of time. The first thing to note is the superposition of the oscillating mode with the unstable mode. The effect of the buoyancy reversal parameters presented in Table 1 is also clearly exposed. As buoyancy reversal is increased from case A0 to A3, the middle unstable layer is relatively heavier (increasing D) and thicker (increasing χ_m), and therefore the growth rate of the unstable mode increases in comparison with the stable oscillation, the distance h_b growing faster during the first 10-15 nondimensional time units. These results agree with those obtained in the linear stability analysis of section 3. The stable case A0 only oscillates, with a period about 10% larger than that predicted by the linear theory and there is a mean growth observed in the figure corresponding to diffusion effects.

The same technique can be used to measure the thickness of the mixing region growing into the upper layer, $h_t(t)$, and the result is shown in Fig. 7. The strong difference with the evolution of the lower thickness $h_b(t)$ of Fig. 6
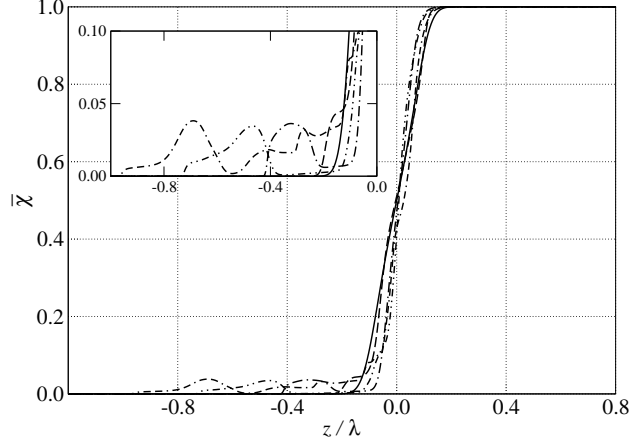
14

Figure 5: Vertical profile of the mean mixture fraction $\bar{\chi}$ for the case A3 every cycle of linear stable mode (same times as shown in Fig. 4): solid, dashed, dot-dashed, dot-dot-dashed and dot-dash-dashed, respectively.
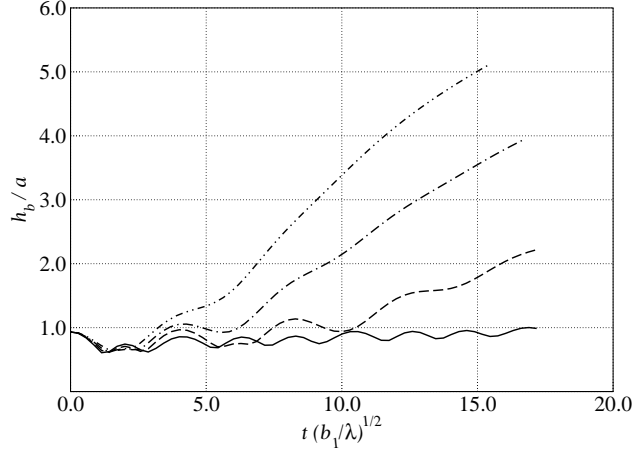

Figure 6: Temporal evolution of the penetration length h_b of the downdrafts for the different cases of Table 1: solid, A0; dashed, A1; dot-dashed, A2; dot-dot-dashed, A3.

is consistent with the mean profiles $\bar{\chi}$ shown in Fig. 5 and the contour plots in Fig. 4, meaning that the upper layer is disturbed only through the oscillating mode, the baroclinically produced vorticity and the diffusion, showing only a steady mild growth of the mean level. This asymmetry in the vertical direction is a major difference with the conventional Rayleigh-Taylor configuration. It merits emphasizing that all cases present the same behavior, and a strong buoyancy reversal like in case A3 does not differ qualitatively from the stable case A0. This means that all the turbulent mixing promoted by the buoyancy reversal is restricted to the lower layer, it is capped and constrained by the strong inversion and there is no enhancement of turbulent entrainment of the upper laminar layer into the mixing region, the mixing region mainly thickens

15

downwards. This result suggests that the pure buoyancy-driven top-cloud mixing layer seems to be more similar to the upper boundary of a Rayleigh-Bérnard convection configuration with this upper boundary free to move and the heat flux towards the lower layer dependent on that motion.
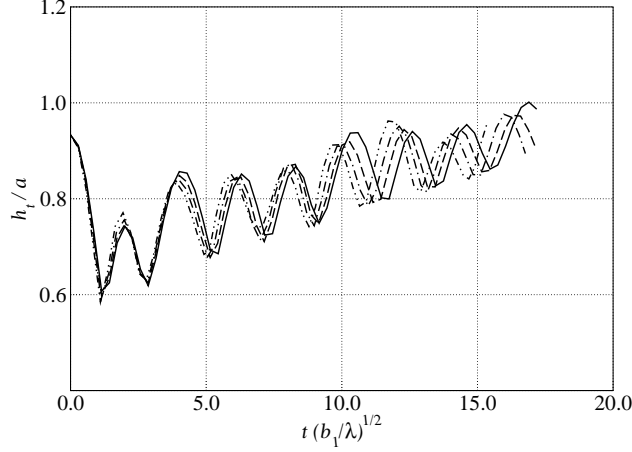

Figure 7: Temporal evolution of the upper perturbation thickness h_t for the different cases of Table 1: solid, A0; dashed, A1; dot-dashed, A2; dot-dot-dashed, A3.

An entrainment velocity with respect to the lower layer can be defined as the temporal derivative of $h_b(t)$. However, detailed quantitative results are influenced by the dominating stable periodic motion, the lack of multi-mode interaction and the two-dimensionality of the problem, thus we defer this analysis to three-dimensional simulations.

5.2 Resolution requirements

The smallest scales in these two-dimensional configurations correspond to the thickness of the diffusive layers, partially represented in Fig. 4, which scale as $(Gr^{1/2} Pr)^{-1/2}$, but the particular resolution required in a simulation depends on the particular numerical algorithm. As already mentioned before, there is a nonzero dilatation caused by the different truncation error between the first- and the second-order finite-differences entering in the solution of the Poisson equation and this quantity can be used to monitor the accuracy of the simulation. Figure 8 shows the temporal evolution of the ratio between the L_2-norms of the dilatation and the vorticity over the whole domain for the different cases.

The case without evaporative cooling A0 has a relative error 10^{-8} and it is therefore very well resolved (the minimum would be round-off error, 10^{-16} using a double precision floating-point system). The presence of buoyancy reversal introduces a dynamically active scale smaller than that observed in the mixture fraction field due to the mapping $b^e(\chi)$, as already discussed, and the effect is observed clearly in Fig. 8 because the dilatation error is increased in three orders of magnitude in comparison with the passive scalar case A0. With the resolution 512×1024 for the Grashof number $Gr = 6.4 \times 10^5$ considered here the dilatation error in the cases with buoyancy reversal remains between 10^{-6}

16

and 10^{-4} times the vorticity magnitude, which might be enough for small-scale analysis in the flow, like probability density functions of derivative fields. When half the resolution is employed, i.e. a mesh 256×512, then the dilatation error increases one order of magnitude; however, differences in the enstrophy fluctuation profile remain below 1% (penetration length $h_b(t)$ curves shown in Fig. 6 are indistinguishable), which suggests that this mesh size is sufficient for the study of large-scale statistics like entrainment rate, Reynolds stresses profiles or budgets of the corresponding transport equations.
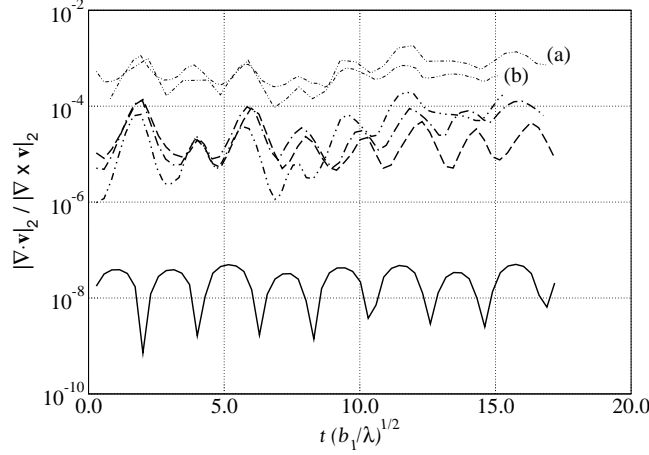

Figure 8: Temporal evolution of the dilatation error measured by the ratio between the L_2-norms of the dilatation and vorticity. Same legend as in Fig. 6 for thick lines. Thin lines correspond to case A3 with: (a) half resolution, (b) no smoothing ($\delta_s = 0$) in the buoyancy function $b^e(\chi)$.

As conclusion from the previous results we can increase the reference Grashof number for the reference grid 512×1024 by a factor of 16, according to the scaling based on $(Gr^{1/2} Pr)^{-1/2}$, and the dilatation error would be about 10^{-3} times the vorticity magnitude having still enough resolution to investigate large-scale quantities. Figure 9 corresponds to case A1 from Fig. 4 but with this new high Grashof number $Gr = 10^7$ plotted over a longer time. The large scale pattern is the same, but the formation of a layer of stronger mixing just bellow the inversion layer is more clearly exposed, in addition to the richer small-scale details allowed by a larger Grashof number. This result can be compared with the case $D = 0.05$ in Siems *et al.* (1990). Note that we define the Reynolds number based on b_1 whereas they base it on Db_1; the case shown in Fig. 9 would have then an equivalent value $\sqrt{D}Re \simeq 6 \times 10^2$, a factor of 3 smaller than the one they use, 2×10^3. However, they report an almost laminar field, quite different from the convoluted picture of Fig. 9 and confirms the necessity of more resolution and high-order schemes to capture the details of the mixing process occurring at the cloud-tops. High Grashof number simulations are further discussed below.

The effect of the smoothing parameter δ_s employed in the definition of $b^e(\chi)$ in Eq. (4) has been also investigated and the dilatation curve for case A3 with the reference fine grid but with $\delta_s = 0$ instead the reference value $\delta_s = \chi_m/16$ is included in Fig. 8. The effect is an increase in the dilatation error of one order
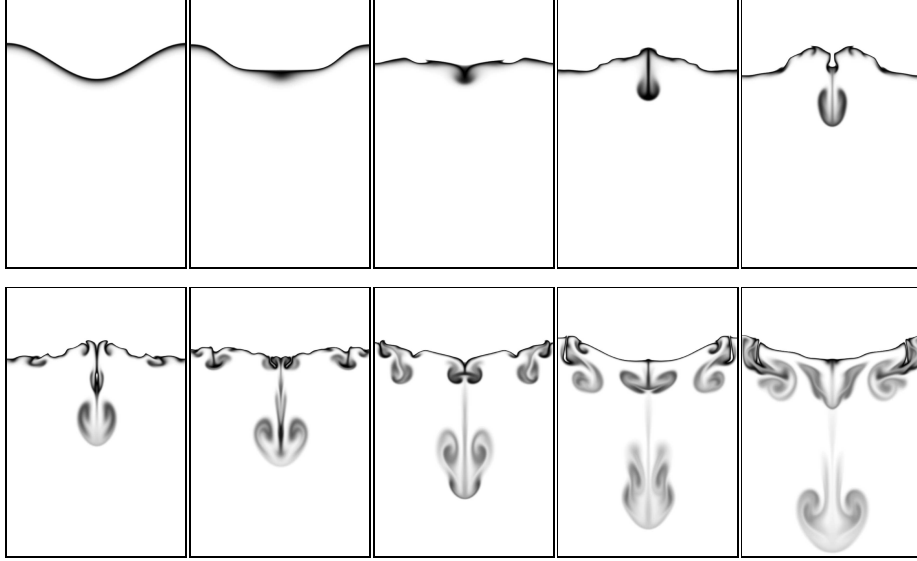
Figure 9: Evolution of the negative buoyancy field for case A1 like in Fig. 4 but during a longer interval. Grashof number $Gr = 10^7$.

of magnitude. On the other hand, the penetration length is higher by about 2% at the final time, which is a measure of the error introduced by the smoothing with δ_s due to the small reduction in the minimum peak of the curve $b^e(\chi)$ in Fig. 1.

5.3 Energy budget

The last statistics to be considered are those related to the energy budget. First, the potential energy is discussed in terms of the buoyancy function b, since the transport equations are normally written in terms of this variable. From the definition $b(\mathbf{x}, t) = b^e(\chi(\mathbf{x}, t))$ and the advection-diffusion transport equation for χ, we obtain the transport equation

$$\frac{\partial b}{\partial t} + \nabla \cdot (\mathbf{v} b) = \kappa \nabla^2 b + S \,, \tag{23}$$

which shows that b is not conserved. If this result is interpreted in terms of the density using Eq. (2), it simply states that mass is not conserved, a well-known defect of the Boussinesq approximation (Lilly, 1996). The source term is

$$S = -\frac{d^2 b^e}{d\chi^2} \kappa |\nabla \chi|^2 = -\frac{Z}{2} \frac{d^2 b^e}{d\chi^2} \,, \tag{24}$$

where $Z = 2\kappa |\nabla \chi|^2$ is the so-called scalar dissipation rate and has dimensions of time^{-1}. When a piecewise-linear approximation is chosen to describe $b^e(\chi)$, its second derivative is proportional to a delta-function $\delta(\chi(\mathbf{x}, t) - \chi_m)$. This case is formally equal to the Burke-Schumann solution of infinitely-fast reacting flows (Burke and Schumann, 1928; Peters, 2000), the buoyancy b playing the role of one reactive scalar with the "flame" sitting at the surface $\chi(\mathbf{x}, t) = \chi_m$

[this "flame front" description has been already used qualitatively by Siems *et al.* (1990)]. The evaporative cooling or heat absorption (S is negative for this configuration) is concentrated on this phase change or evaporation surface. For the approximation Eq. (4) employed here [already used in DNS of reacting flows by Pantano *et al.* (2003)] the curvature of the buoyancy function is

$$\frac{d^2 b^e}{d\chi^2} = b_1 \left(\frac{1+D}{1-\chi_m} + \frac{D}{\chi_m} \right) \frac{1}{4\delta_s} \left[\cosh \left(\frac{\chi - \chi_m}{2\delta_s} \right) \right]^{-2} .$$

In the expression above, the term inside the first parentheses is the difference in the slopes of the piecewise-linear profile, which gives the strength of the evaporative cooling, and the rest can be interpreted as a delta-sequence that converges to the delta-function as $\delta_s \to 0$. A compromise in the value of δ_s, small enough to mimic a localized heat absorption zone but large enough to be resolved by the grid, has already been discussed.

Multiplying Eq. (23) by the vertical coordinate z we obtain

$$\frac{\partial(bz)}{\partial t} + \nabla \cdot (\mathbf{v}bz) = bw + \kappa z \nabla^2 b + zS , \qquad (25)$$

and taking the mean over horizontal planes leads to

$$\frac{\partial(\bar{b}z)}{\partial t} + \frac{\partial(\overline{bw}z)}{\partial z} = B + \kappa \left[\frac{\partial}{\partial z} z \frac{\partial \bar{b}}{\partial z} - \frac{\partial \bar{b}}{\partial z} \right] + z\bar{S} , \qquad (26)$$

where the turbulent buoyancy flux is given by $B(z,t) = \overline{w'b'}$ and the condition $\bar{w} = 0$ satisfied in our configuration has been used. The evolution equation for the total integrated potential energy is then

$$\frac{d}{dt} \left(- \int_{-\infty}^{\infty} z\bar{b}dz \right) \quad = \quad - \int_{-\infty}^{\infty} B dz \quad + \quad \kappa b_1 \quad - \quad \int_{-\infty}^{\infty} z\bar{S}dz \quad . \quad (27)$$

The first line in the equation above corresponds to the balance we would obtain in the exact formulation of the problem from the mass conservation equation: the integrated potential energy changes only through the total buoyancy flux. In contrast, in the current Boussinesq limit we obtain two additional sources. Note that the balance in Eq. (27) is independent of the reference used to measure vertical distances, but the time change of the integrated potential energy or the contribution from S individually do depend on that arbitrary reference. Last, the integral of $\bar{b}$ as it is in the left-hand side does not converge since $\bar{b} = b_1$ far above in the upper layer. However, the equation can be written in terms of $\bar{b} - f(z)$ for any constant function $f(z)$, and we can choose $f(z) = b^e(\chi_i(z))$, χ_i from Eq. (9), without loss of generality in order to regularize the problem.

The turbulent buoyancy flux represents the transfer of energy between the turbulent kinetic energy and the potential energy, and it is easy to show that the total mechanical energy evolves according to the equation

$$\frac{d}{dt} \left[\int_{-\infty}^{\infty} (|\mathbf{v}'|^2/2 - z\bar{b})dz \right] \quad = \quad - \int_{-\infty}^{\infty} \bar{\epsilon}dz \quad + \quad \kappa b_1 \quad - \quad \int_{-\infty}^{\infty} z\bar{S}dz \quad , \quad (28)$$

where ϵ is the turbulent dissipation rate [$\epsilon = \nu\, v'_{i,j}(v'_{i,j} + v'_{j,i})$ in Cartesian coordinates using index notation]. The apostrophe indicates turbulent fluctuations.

19

Table 2: <u>Simulation series B. Grashof number</u> $Gr = 10^7$.

	D	χ_m	δ/λ	$(a/2)/\lambda$
B0	-	-	0.025	0.10
B1	0.031	0.09	0.025	0.10
B2	0.062	0.09	0.025	0.10
B3	0.031	0.18	0.025	0.10
B4	0.031	0.09	0.050	0.10
B5	0.031	0.09	0.025	0.05

The term κb_1 represents a linear diffusion source of potential energy which is always present, linear meaning that it contains the contribution from the linear part of the buoyancy function $b^e(\chi)$ varying between 0 and b_1 [see Eq. (4) and Fig. 1]. The source term S contains the nonlinear contribution, since it is proportional to the curvature of the buoyancy function, by definition Eq. (24). Note that the linear source term κb_1 is always present, even in a one-dimensional purely diffusion case without buoyancy reversal, and represents a constant linear growth in time.

A new series of simulations with a Grashof number $Gr = 10^7$, series B described in Table 2, has been performed in order to study the energy equation. The different cases are defined by varying each of the nondimensional parameters identified through the paper instead of modifying the water content and temperature as was done in series A, Table 1. The reference case is B1 and corresponds again to the experimental data taken from DYCOMS-II (Stevens *et al.*, 2003), i.e. it is the same as case A1 with a higher Grashof number (see Fig. 9). The vertical size of the domain has been extended to 2.5λ in order to allow longer simulations.

Figure 10 shows the balance of the integrated energy Eq. (28). It has been integrated in time to observe the accumulation of numerical errors,

$$\left[\int_{-\infty}^{\infty}(|\mathbf{v}'|^2/2 - z\bar{b})dz\right]_0^t = \kappa b_1 t - \int_0^t \int_{-\infty}^{\infty} z\bar{S}dzd\tau - \int_0^t \int_{-\infty}^{\infty} \bar{\epsilon}dzd\tau \ , \quad (29)$$

where the terms are, from left to right, the mechanical energy, the linear source of potential energy, the nonlinear source due to S, and the energy dissipation.

The results show that the linear source κb_1 contributes positively to the overall balance, in particular increasing the potential energy through the diffusion of heavy fluid from the bottom to the top, and the rate of this contribution is constant in time and independent of the buoyancy reversal parameters D and χ_m, and of the geometry of the initial condition δ and a. The other two terms contribute negatively: the nonlinear source term tends to reduce the potential energy because of the generation of negatively buoyant (heavy) parcels in the lower layer, and the turbulent dissipation because it represents the removal of turbulent kinetic energy by definition. The last curve in Fig. 10 depicts the difference between the left-hand side and the right-hand side of Eq. (29), which quantifies the numerical errors introduced by the algorithm. It is observed that they are indeed negligible, decreasing to less than 1% of the turbulent dissipation, and validates once more the numerical scheme used in the study.

The source term S is further investigated. First, the accumulated integral value of the this source is computed, which from Eq. (23) is related to the
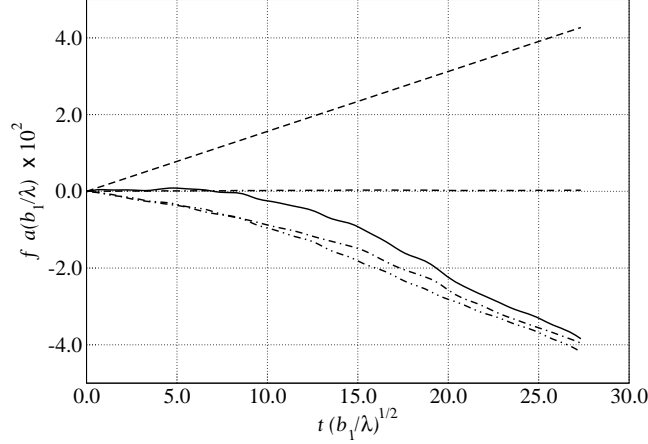
Figure 10: Energy budget according to Eq. (29): solid, mechanical energy; dashed, linear source; dot-dashed, nonlinear source; dot-dot-dashed, energy dissipation. The accumulated numerical error is represented by the dot-dash-dashed line.

evolution of the integrated buoyancy

$$\left[\int_{-\infty}^{\infty} \bar{b} dz \right]_0^t = - \int_0^t \int_{-\infty}^{\infty} \bar{S} dz d\tau \ . \tag{30}$$

This term is shown in Fig. 11 for the different cases of Table 2, normalized by the strength of the evaporative cooling $b_1[(1+D)/(1-\chi_m)+D/\chi_m]$. With this normalization and from Eq. (24), this term is approximately proportional to the accumulated integral value of the scalar dissipation rate Z conditioned on the evaporation surface $\chi(\mathbf{x},t) = \chi_m$, and therefore very related to the turbulent mixing generated by the motion. In fact, the curves shown in Fig. 11 show an increase in the accumulated buoyancy as more forcing is imposed, by increasing D or χ_m or a. The parameter δ is also consistent with this interpretation because the higher δ for a given a, the smoother the initial buoyancy profile and the smaller the initial potential energy set in the problem.

Last, it is also interesting to calculate where in the domain the evaporative cooling is most concentrated, which is related to the source term of the energy equation. It has been observed in Fig. 10 that the nonlinear source term S decreases the integrated potential energy, but this interpretation really depends on the vertical reference position taken to calculate the potential energy, although the balance between them, which is equal to the remaining terms in Eq. (27), is of course independent of that reference. A useful quantity for that purpose is the instantaneous centroid of the function $S(\mathbf{x},t)$

$$z_s(t) = \frac{\int_{-\infty}^{\infty} z \bar{S} dz}{\int_{-\infty}^{\infty} \bar{S} dz} \ . \tag{31}$$

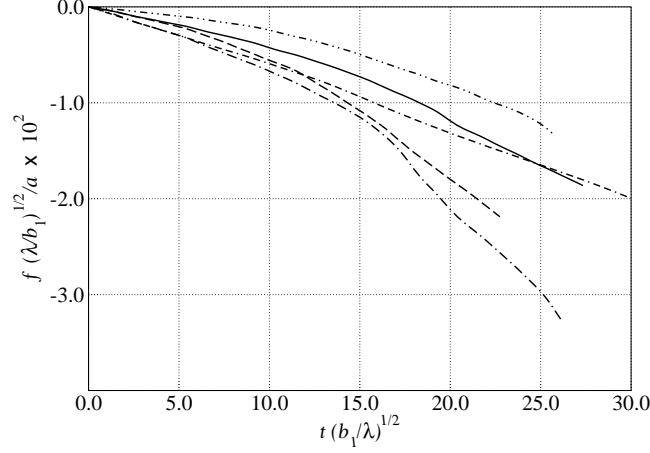This location can be used as reference for the definition of the potential energy,

21

Figure 11: Normalized integrated buoyancy [see Eq. (30) and text] for different cases: solid, reference, B1; dashed, double D, B2; dot-dashed, double χ_m, B3; dot-dot-dashed, double δ, B4; dot-dash-dashed, half a, B5.

if desired, which allows Eq. (27) to be written as

$$\frac{d}{dt}\left[-\int_{-\infty}^{\infty}(z - z_s(t))\bar{b}dz\right] = -\int_{-\infty}^{\infty}Bdz + \kappa b_1 + \frac{dz_c}{dt}\int_{-\infty}^{\infty}\bar{b}dz \quad (32)$$

introducing a velocity dz_c/dt. The energy equation Eq. (28) can be correspondingly rewritten, if desired.
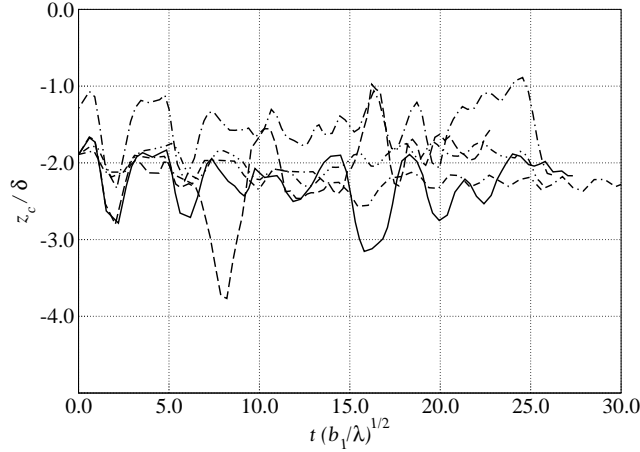

Figure 12: Centroid of the function $S(\mathbf{x}, t)$ according to definition Eq. (31). Same legend as in Fig. 11.

The evolution of $z_c(t)$ is therefore of interest and it is shown in Fig. 12 for the different cases. The first thing to note is that it is relatively constant in time, meaning that it presents oscillations but the mean remains constant. Hence, the mean position of the evaporative cooling source remains located between 1δ

22

and 3δ below the reference position of the stable mode, and the decrease in the nonlinear source term of the energy equation in Fig. 10 is mainly determined by the evolution of the source term S itself shown in Fig. 11. After these parcels of relatively heavy mixture have been generated, mixing homogenizes the field b, mixing that can be generated either by the oscillating mode, dominant in the two-dimensional single-mode cases considered in this paper, or by the downdrafts of the heavy mixtures themselves. The influence of δ in the problem has been determined, but the role of the other parameters cannot be really deduced from Fig. 12 for the current configuration.

5.4   Discussion

The objective of this section has been the validation of the incompressible code, extension of the linear stability analysis and the explanation of the flow characteristics based on the mixture fraction and energy statistics. However, it is emphasized that the detailed quantitative analysis has necessarily to be discussed with three-dimensional broadband turbulent simulations because the mixing is different. There are several questions that appear naturally after the results presented in this paper. For instance, how does the energy budget of Fig. 10 evolve in reality? Inviscid scaling arguments would suggest that the linear term would decrease compared to the other two as the Grashof number is increased. Is there any relation between the evolution of the integrated source of buoyancy S, with dimensions of velocity, with that of dh_b/dt in Fig. 11? What is the role and evolution of the stable mode in the actual problem? The extension of this study to three-dimensional situations will answer these questions and will help to gain further useful knowledge of the cloud-top configuration before introducing more phenomena like mean shear or turbulent layers.

6   Conclusions

The buoyancy-driven cloud-top mixing layer has been investigated in this paper. Linear stability analysis of a simplified model consisting of three uniform inviscid layers with different densities has been presented. It identifies the two time-scales of the system $|\sigma_u|^{-1}$ and $|\sigma_s|^{-1}$, shows the condition of buoyancy reversal instability ($D > 0$) and provides an interpretation of the buoyancy reversal parameter D as a measure of the ratio between those two time-scales. For small values of D the growth rate of the unstable mode scales as $\sqrt{D}$ times that of the stable one. The effect of the second buoyancy reversal parameter χ_m is retained through the dependence of the solution on the thickness of the intermediate layer, which can be estimated by $\delta(\chi_m+D)/(1+D)$ if δ represents an appropriate thickness of the interface defined in terms of the mixture fraction field. The unstable growth rate increases with respect to the stable one monotonically with this thickness towards an asymptotic value.

The nonlinear regime has been illustrated through single-mode two-dimensional simulations, a study that has also been used to explore the consistency and convergence of the numerical methods employed. Spatial derivatives are based on sixth-order compact schemes, time advancement employs a forth-order low-storage Runge-Kutta algorithm and the Poisson equation is solved by Fourier transforming the equation in the horizontal periodic planes and then solving

the resulting sequence of one-dimensional equations along the vertical direction using again sixth-order compact schemes. The truncation error introduced by substituting the two first-order finite-difference operators by one second-order finite-difference, observed in the dilatation, has been used to show resolution requirements. The balance of the terms in the evolution equation of the integrated energy has also confirmed the accuracy of the numerical scheme, achieving a Grashof number $Gr = 10^7$ with a grid size 512×1024.

The two-dimensional simulations agree with previous work on the topic in that a runaway instability of the system does not become evident, but show that a significant increase in the resolution of small-scale mixing is required, in special for the cases with small values of D. Statistics of the mixture fraction and energy budget show that there is no enhancement of entrainment of upper fluid by evaporative cooling for the low levels of buoyancy reversal typical of stratocumulus tops, and these heat absorption effects are mainly restricted to the lower layer. How buoyancy reversal modifies an already existing turbulent entrainment caused for instance by an imposed shear or a lower turbulent layer remains an open question, but buoyancy reversal alone seems to be unable to break the cloud, it simply homogenizes the lower layer faster. It has also been shown that the associated buoyancy source term is mainly localized below the stable stratification at a distance comparable to the initial thickness of the mixture fraction field, and the motion generated by the downdrafts mixes these negatively buoyant parcels with the environmental fluid of the lower layer. Three-dimensional simulations are still of interest to obtain more detailed quantitative results before considering the shear-driven case.

Acknowledgement

References

Burke SP, Schumann TEW. 1928. Diffusion flames. *Ind. Eng. Chem.* **20**(10): 998–1004.

Cook AW, Dimotakis PE. 2001. Transition stages of Rayleigh-Taylor instability between miscible fluids. *J. Fluid Mech.* **443**: 69–99.

Corrsin S, Kistler A. 1955. Free-stream boundaries of turbulent flows. Technical Report 1244, NACA, Washington DC.

Deardorff JW. 1980. Cloud top entrainment instability. *J. Atmos. Sci.* **37**: 131–147.

Dimotakis PE. 2005. Turbulent mixing. *Annu. Rev. Fluid Mech.* **37**: 329–356.

Fernando HJS. 1991. Turbulent mixing in stratified fluids. *Annu. Rev. Fluid Mech.* **23**: 455–493.

Flatau PJ, Walko RL, Cotton WR. 1992. Polynomial fits to saturation vapor pressure. *J. Appl. Meteor.* **31**: 1507.

Grabowski WW. 1995. Entrainment and mixing in buoyancy-revesing convection with applications to cloud-top entrainment instability. *Q. J. Roy. Meteorol. Soc.* **121**: 231–253.

Gresho PM. 1991. Incompressible fluid dynamics: some fundamental formulation issues. *Annu. Rev. Fluid Mech.* **23**: 413–453.

Hunt JCR, Eames I, Westerweel J. 2006. Mechanics of inhomogeneous turbulence and interfacial layers. *J. Fluid Mech.* **554**: 499–519.

Jacobs JW, Dalziel SB. 2005. Rayleigh-Taylor instability in complex stratifications. *J. Fluid Mech.* **542**: 251–279.

Kuo H, Schubert WH. 1988. Stability of cloud-topped boundary layers. *Q. J. Roy. Meteorol. Soc.* **114**: 887–916.

Lele SK. 1992. Compact finite difference schemes with spectral-like resolution. *J. Comput. Phys.* **103**: 16–42.

Lilly DK. 1968. Models of cloud-topped mixed layers under strong inversion. *Q. J. Roy. Meteorol. Soc.* **94**: 292–309.

Lilly DK. 1996. A comparison of incompressible, anelastic and boussinesq dynamics. *Atmos. Res.* **40**: 143–151.

Mellado JP, Sarkar S, Zhou Y. 2005. Large-eddy simulation of Rayleigh-Taylor turbulence with compressible miscible fluids. *Phys. Fluids* **17**: 076 101.

Mellado JP, Wang L, Peters N. 2008. Gradient trajectory analysis of a scalar field with external intermittency. *Submitted to J. Fluid Mech.* .

Pantano C, Sarkar S, Williams FA. 2003. Mixing of a conserved scalar in a turbulent reacting shear layer. *J. Fluid Mech.* **481**: 291–328.

Peters N. 2000. *Turbulent combustion*. Cambridge University Press.

Ramaprabhu P, Andrews MJ. 2004. Experimental investigation of Rayleigh-Taylor mixing at small Atwood numbers. *J. Fluid Mech.* **502**: 233–271.

Randall DA. 1980. Conditional instability of the first kind upside-down. *J. Atmos. Sci.* **37**: 125–130.

Sharp DH. 1984. An overview of Rayleigh-Taylor instability. *Physica D* **12**: 3–18.

Shy SS, Breidenthal RE. 1990. Laboratory experiments on the cloud-top entrainment instability. *J. Fluid Mech.* **214**: 1–15.

Siems ST, Bretherton CS. 1992. A numerical investigation of cloud-top entrainment instability and related experiments. *Q. J. Roy. Meteorol. Soc.* **118**: 787–818.

Siems ST, Bretherton CS, Baker MB, Shy S, Breidenthal RE. 1990. Buoyancy reversal and cloud-top entrainment instability. *Q. J. Roy. Meteorol. Soc.* **116**: 705–739.

Stevens B. 2002. Entrainment in Stratocumulus topped mixed layers. *Q. J. Roy. Meteorol. Soc.* **128**: 2663–2690.

Stevens B, D-H-Lenschow, Faloona I, Moeng CH, Lilly DK, Blomquist B, Vali G, Bandy A, Campos T, Gerber H, Haimov S, Morley B, Thorton C. 2003. On entrainment rates in nocturnal marine Stratocumulus. *Q. J. Roy. Meteorol. Soc.* **129**(595): 3469–3493.

Tritton DJ. 1988. *Physical fluid dynamics*. Oxford Science Publications.

Turner JS. 1973. *Buoyancy effects in fluids*. Cambridge University Press.

Williamson JH. 1980. Low-storage Runge-Kutta schemes. *J. Comput. Phys.* **35**: 48–56.

Wilson RV, Demuren AO, Carpenter M. 1998. Higher-order compact schemes for numerical simulation of incompressible flows. Technical Report CR-1998-206922, NASA Langley Research Center.

Wunsch S. 2003. Stochastic simulations of buoyancy reversal experiments. *Phys. Fluids* **15**(6): 1442–1456.

Yamaguchi T, Randall DA. 2008. Large-eddy simulation of evaporatively driven entrainment in cloud-topped mixed layers. *J. Atmos. Sci.* **65**: 1481–1504.

Yang Y, Zhang Q. 1993. General properties of a multilayer stratified fluids systems. *Phys. Fluids A* **5**(5): 1167–1181.